PERGAMON

International Journal of Solids and Structures 37 (2000) 1765–1791

INTERNATIONAL JOURNAL OF SOLIDS and STRUCTURES

www.elsevier.com/locate/ijsolstr

# Composite failure under combined compression and shear

T.J. Vogler, S.-Y. Hsu, S. Kyriakides*

*Research Center for Mechanics of Solids, Structures and Materials, The University of Texas at Austin, WRW 110, TX 78712, Austin, USA*

Received 7 July 1998; in revised form 2 November 1998

**Abstract**

The effect of a superimposed shear stress on the axial compressive strength of aligned fiber composites is investigated through a combination of experiments and analysis. Experiments were conducted on flat coupons using a custom biaxial testing facility. Shear and compression were found to interact strongly. The interaction failure envelope follows approximately a linear trend along the line joining the critical stress at zero shear on one axis and the shear strength on the other. The 2-D and 3-D micromechanical models used previously to predict the compressive strength are modified to include the shear. In the models the composite has a sinusoidal imperfection which is uniform across the microsection width. The imperfection characteristics are chosen so that the calculated critical stress at zero shear corresponds to the measured strength. The models are shown to capture well the interaction between shear and compression. Calculated failure envelopes are in good agreement with the experimental results. For all combinations of shear and compression considered, deformation localizes into a narrow band of highly bent fibers after the critical state. The band initially is normal to the axial load but broadens and rotates as the solution is followed deeper into the postfailure regime as it did for pure compression. Important aspects of proper testing and modeling are discussed, and recommendations are given for design including a critical review of a simpler model in which the fibers do not deform. 

*Keywords:* Fiber composites; Failure; Compression and shear

## 1. Introduction

It is now commonly accepted that the failure of aligned fiber composites is due to buckling of the fibers in the inelastic matrix. This was first recognized by Argon (1972) and later by Budiansky (1983). They observed that even in unidirectional material the fibers have small misalignments and under axial compression the matrix can develop shear. Typical polymeric matrices used in advanced composite

* Corresponding author.
*E-mail address:* skk@mail.utexas.edu (S. Kyriakides)

0020-7683/00/$ - see front matter 
PII: S0020-7683(98)00323-0

materials yield at relatively low shear stresses, and, as a consequence, the composite shear response is also nonlinear with relatively low yield stress. For fiber misalignments of the order of one to two degrees, the material can yield in shear at compressive stresses of the order of 50% of the tensile strength. The reduction in shear modulus caused by this yielding causes shear buckling of the fibers.

Kyriakides et al. (1995) and Kyriakides and Ruff (1997) idealized the composite as a two-dimensional solid with alternating layers representing elastic fibers and inelastic matrix with an initial waviness. The properties of the constituents were selected so that the shear response of the model material matched that of an AS4/PEEK composite. They then showed that when a representative microsection of this model material is compressed it develops a limit load instability essentially for the reasons given by Argon and Budiansky. Following the limit load, deformation was shown to localize in a narrow inclined band crossing the specimen. The fibers inside the band bend and rotate very much like in kink bands reported from compressive failure experiments.

In a similar effort, Hsu et al. (1998) considered a model composite with circular elastic fibers with a hexagonal distribution inside an inelastic matrix. The model composite was again assigned the same shear response as the actual material. Under compression this model behaved in a manner similar to the two-dimensional model developing a limit load followed by localized bending in well defined narrow bands across the microsection.

Based on these findings it was concluded that the most appropriate version of the original model of Budiansky mentioned above (which was taken much further in Budiansky and Fleck, 1993) is the zero kink band angle version. In the simplest version of the model the fibers are assumed to be inextensional and uniformly inclined to the line of loading by a small angle $\theta_0$ as shown in Fig. 1. Simple equilibrium considerations of the element relate the applied stress ($\sigma$) to the induced shear ($\gamma$) by

$$\sigma = \frac{\tau(\gamma)}{\theta_0 + \gamma} \tag{1}$$

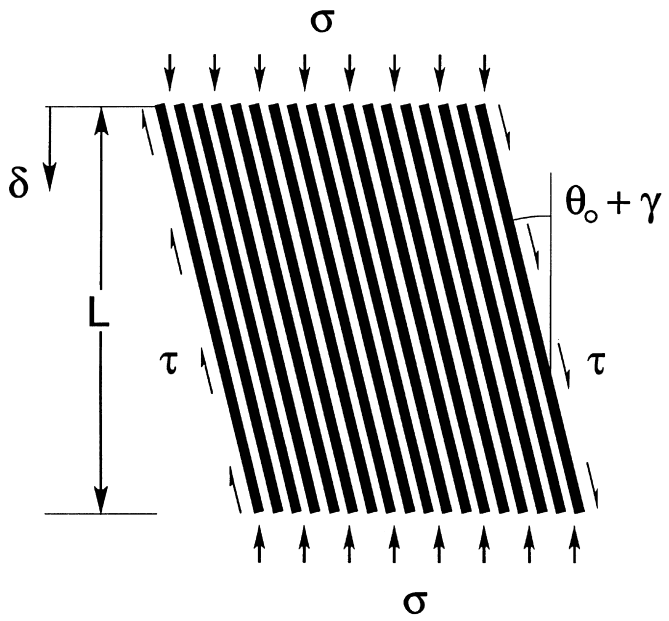


Fig. 1. Idealized composite used in the straight fibers model.

where $\tau(\gamma)$ is the nonlinear response of the composite in shear ($\gamma$ is assumed to be small). (Eqn (1) was also reported in Chatterjee and McLaughlin, 1979 and was used by Schapery, 1992). The material nonlinearity in the numerator and the geometric nonlinearity in the denominator interact to cause a limit load in $\sigma$ at some value of $\gamma$. This limit load is taken to represent the strength of the composite.

Hsu et al. (1998) compared strength predictions from eqn (1) with those from the two- and three-dimensional numerical models in which the sinusoidal imperfection was assumed to be uniformly distributed and to have an amplitude corresponding to $\theta_0$. It was shown that, provided the shear responses in the three models are the same, the predicted strengths are similar. For misalignment angles less than one degree, the extensionality of the fibers plays a role and, as a result, eqn (1) overestimates the strength.

Budiansky and Fleck (1993) showed that shear applied simultaneously with axial compression can reduce the strength of aligned composites quite significantly (see also Slaughter et al., 1993). Jelf and Fleck (1994) confirmed this strong interaction in experiments on pultruded fiber-epoxy (EXAS HSI/DX 6002) composite tubes tested under combined axial compression and shear. Here we revisit the problem and analyze it through extended versions of the 2-D and 3-D models used in Hsu et al. (1998) for pure axial compression and by a version of the straight fiber model of Budiansky and Fleck. It will be shown that for this case also the numerical results support that the most appropriate version of the straight fiber model of Budiansky and Fleck is one with zero kink band inclination. The models are evaluated by comparing the predicted interaction failure envelopes with new experimental results on the same AS4/PEEK composite used in our previous work.

## 2. Experiments

### 2.1. Experimental set-up

The effect of shear on the compressive response and failure was first investigated experimentally. The

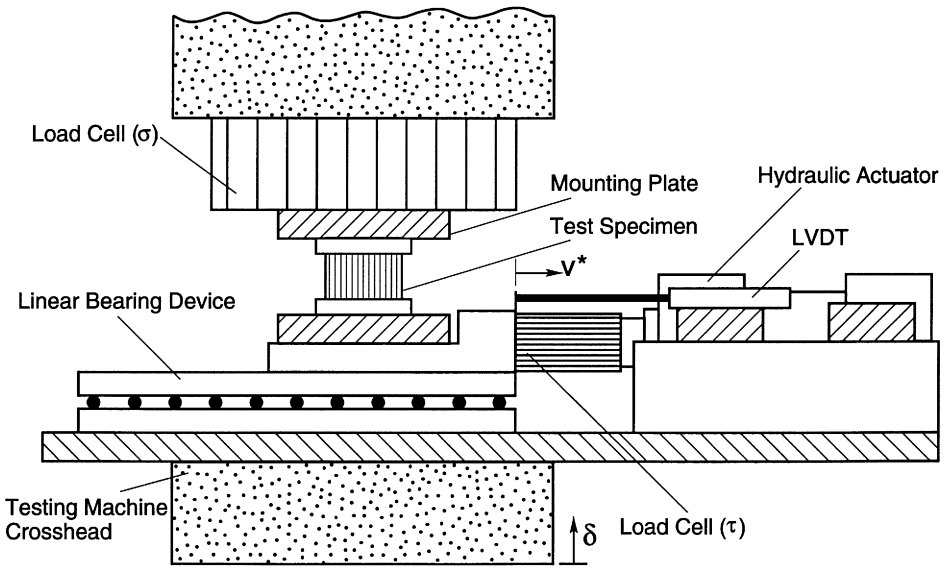


Fig. 2. Side view of device used for combined compression-shear loading of composite specimens.

material used was the same AS4/PEEK unidirectional composite used in our previous studies in order to exploit the existing material characterization data essential for the analyses that follow. The cleanest experimental method for applying pure shear is twisting of thin-walled tubes. Our composite is in the form of a 0.75 in (19 mm) plate which limited the size of tubes we could make to impractically small diameters. For this reason, we opted for a compromise setup involving a $2 \times 2 \times 0.125$ in ($50.8 \times 50.8 \times 3.18$ mm) square plate compressed while simultaneously sheared by end loads. The plate is tested in a special device shown schematically in Fig. 2 developed for measuring the inelastic behavior of materials under compression and shear. In such tests, edge effects and axial stress non-uniformity are limited by employing a relatively long strip of material much like in a rail shear test. In the present tests, the specimen aspect ratio could not be too large in order to ensure that an inclined kink band initiated from one of the plate free edges would stay within the test section on reaching the other free edge.

The device is mounted onto a universal testing machine which applies the compression. Shear is applied by a one inch stroke, 10 kip (44 kN) capacity hydraulic actuator mounted onto a stiff carrier plate which in turn is attached to the crosshead of the testing machine. The top of the specimen is attached via a special end plate to the load cell of the axial testing machine which is very stiff under a side load. A similar mounting plate at the bottom of the specimen is attached to a linear bearing connected to the horizontal actuator as shown in the figure. The bearing allows horizontal motion of the bottom of the specimen with minimal friction even at high axial loads. The horizontal load is monitored by a load cell connected between the actuator and the bearing; the horizontal displacement ($v^*$) is monitored by an LVDT displacement transducer. Both axes of loading can be operated in either load or displacement control. The independence of control for the shear and the axial loads allows arbitrary choice of path in the biaxial stress ($\tau - \sigma$) or strain ($\gamma - \varepsilon$) space.

The top and bottom ends of the specimen are bonded with a high strength adhesive (Hysol XEA 9359.3) to 0.4 in (10 mm) thick steel plates as shown in Fig. 3. The thickness of the adhesive is 0.007 in (0.178 mm). A fillet with a radius of approximately 0.04 in (1 mm) is left at the edge of the adhesive to reduce the local stress concentration. Prior to bonding, the specimen is roughened in the bond area with sandpaper and cleaned. A special aligning jig is used during the bonding process to ensure that the assembly consisting of the mounting plates, the specimen and the end plates are kept aligned. One of the

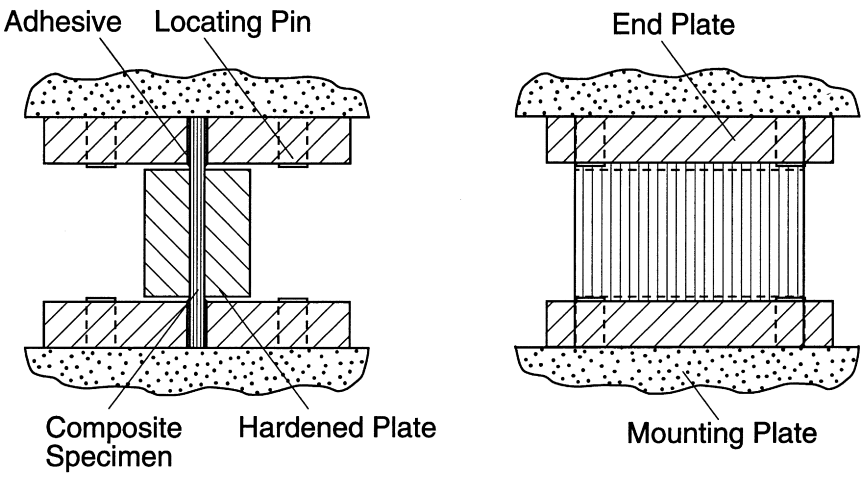


Fig. 3. Details of mounting for shear-compression specimen.

objectives of the tests was to establish any differences induced by shear to the characteristics of kink bands that develop as the material fails. As in our previous work (Vogler and Kyriakides, 1997), this was accomplished by laterally confining the plate by clamping on either side of it 0.4 in thick, hardened steel plates with lubricated ground surfaces. The clamping force applied was relatively small to keep friction to a minimum.

When assembled, the specimen has a test section of $1.2 \times 2 \times 0.125$ in ($30 \times 50 \times 3.18$ mm). The aspect ratio of the test section is relatively small and, as a result, some stress nonuniformity develops due to the free edges. An alleviating factor is the fact that due to the very anisotropic properties of such composites the shear stresses that are applied are relatively small compared to the axial stresses. The axial strength of the material is approximately 175 ksi (1.2 GPa). The maximum shear stress the material can sustain is approximately 12 ksi (83 MPa). At the maximum shear stress applied in the tests of 10 ksi (69 MPa) the axial stress required to fail the material is of the order of 50 ksi (345 MPa). This big difference in the two stresses means that the nonuniformity induced in the axial stress due to the shear load is relatively modest compared to the mean axial stress and is limited to the neighborhood of the free edges.

In addition to this nonuniformity of axial and shear stress, the specimen has some stress concentrations at the interface of the bonded end-plates and the specimen. Finite element analyses of the initial elastic stress states showed that the maximum stress concentration in the axial stress at the corners of these discontinuities was of the order of 1.5. This, however, was limited to a very small local zone. As a result of these limitations of the test set up, the biaxial strength envelope we present can be considered to be a lower bound of the true material failure envelope.

### 2.2. Experimental results

Two different loading histories were used in the biaxial tests. In the first, the specimen was sheared to a predetermined level under load control. Then, with the shear load fixed, the specimen was compressed at a prescribed constant displacement rate ($\dot{\delta}/L$) of $6.7 \times 10^{-5}$ s$^{-1}$ (similar to rates used in uniaxial compression tests in Kyriakides et al., 1995). This loading history will be designated as $\tau \rightarrow \varepsilon$. In the second loading path, the specimen was first compressed to a predetermined value of axial stress and then it was sheared under displacement control to failure at the rate $\dot{\nu}^*/L$ of $3 \times 10^{-5}$ s$^{-1}$ while the axial stress was kept fixed. This will be designated as the $\sigma \rightarrow \gamma$ loading path. The nonlinear shear response of the composite is rate dependent and, as a result, the measured strength is affected to some degree by the rate of loading (Vogler and Kyriakides, 1998). Here, for expediency, we examine failure only at one set of low strain rates.

The strength of the material under pure uniaxial compression was established first using conventional cylindrical specimens with a uniform test section. They were tested in the axisymmetric set-up shown in Fig. 1 of Kyriakides et al., 1995 which was designed to exhibit only modest stress-concentrations. The strengths measured in three such tests were 171.7, 176.5 and 187.9 ksi (1.184, 1.1217, 1.296 GPa) which are comparable to the values we reported in 1995 from tests on an earlier batch of the same material. The compressive response exhibits a very mild nonlinearity. In this set-up, the specimen fails suddenly and catastrophically with rupture usually occurring in the test section.

The shear response of the material is highly nonlinear (see Fig. 11 later). Depending on the test set-up used and the integrity of the test specimen, shear strains as high as 10% have been achieved. At such high strains the tangent modulus is quite small. We performed several shear tests on filament wound thin-walled AS4/PEEK tubes. We also sheared several long strips, cut from the mother plate, in the device shown in Fig. 2. While the shear responses were quite similar the failure strains varied from 4 to 10% as the specimens failed due to various experimental factors. The failure stress at the highest strain

we recorded was 13.47 ksi (92.9 MPa); this will be taken to be a lower bound of the material strength in shear.

*2.2.1. $\tau \rightarrow \varepsilon$ path*

We first examine failure for the $\tau \rightarrow \varepsilon$ loading path. Tests were performed at shear stresses ranging from 2 to 10 ksi (13.8–68.7 MPa). Shear was applied first and fixed at the desired level. The specimen was then compressed at the constant displacement rate given above. Compression increased the shear strain in the specimen further and, as a result, the horizontal displacement $v^*$ increased. At some value of axial compression the initial shear coupled with the additional amount induced by compression reduce the shear modulus to a level that allows inelastic collapse of the specimen. Since the shear stress was prescribed, failure was sudden and catastrophic with the machine shutting off when a certain value of the displacement $v^*$ was exceeded. Failure resulted in the formation of one or two kink bands in the test section. The kink bands initiated from one or both of the corners of the test section where the highest stress concentrations are. The maximum axial stress recorded is taken to be the critical stress ($\sigma_C$) for the particular value of shear stress applied.

Eleven such experiments were conducted. The critical stresses measured are plotted against the applied shear stress ($\tau_\infty$) in Fig. 4. The figure also includes the failure stresses from three uniaxial compression tests and the ultimate shear strength of the composite in pure shear recorded in the other type of test mentioned above. As expected from the work of Budiansky and Fleck (1993), the interaction between the two stresses is strong resulting in the failure points falling along a nearly diagonal line joining the strengths on the two axes (pure compression and pure shear). The trend of the results is also similar to that of results reported in Jelf and Fleck (1994) from torsion-compression tests on a different composite (a small difference is that they performed several tests at the same value of shear and reported the average compressive strengths measured thus reducing the scatter of their results).

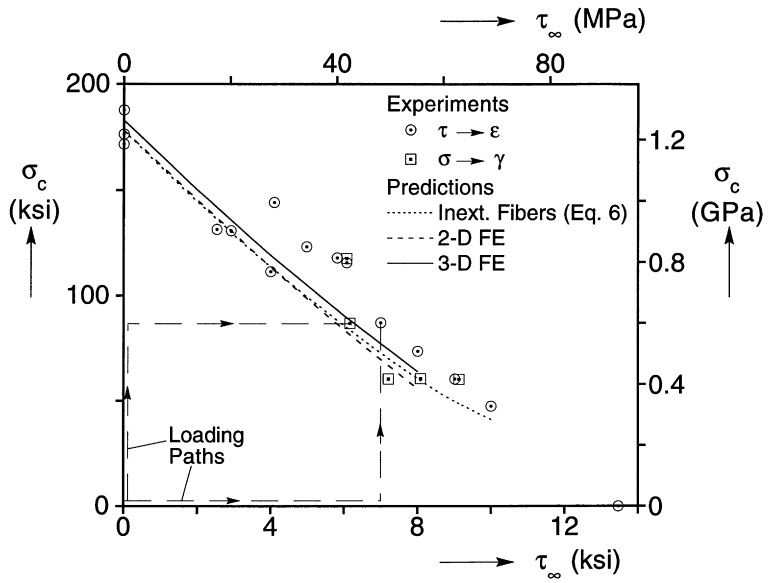


Fig. 4. Comparison of compressive strength under shear loading from experiments and three models.

The results exhibit some scatter which can be attributed to several factors. As discussed in Kyriakides and Ruff (1997), our composite has two types of fiber imperfections. The first type is introduced in the plane of the ply during the manufacture of the prepreg. The second is introduced during the curing of the laminate in the stacking plane. Although both have distinct spatial distributions, neither has a preferred orientation. The imperfections in the stacking plane were found to occur in 'islands' which are distributed throughout the mother plate. They were estimated to have diameters as large as 0.6 in (15 mm). When the plate is cut and sliced to extract our $2 \times 2 \times 0.125$ in plate specimens, some of the specimens may be free of this type of imperfection and others may suffer severely from it. This causes variation in the apparent strength of individual specimens.

By examining the orientation of the fibers on the surfaces of the specimens, we noticed that the cutting can introduce an additional misalignment which is of the order of $0.5^\circ$. The orientation of this misalignment was not always recorded. Whereas in pure compression this additional misalignment always causes a reduction in the strength, under shear, this misalignment will result in a reduction in strength if oriented in the direction of the shear but will cause an increase in strength if oriented opposite to the direction of the shear. This uncertainty in the orientation of this misalignment adds to the scatter of the failure stresses in Fig. 4. We will illustrate this point further with the help of models in §4. This type of imperfection should not be present in the pultruded material used by Jelf and Fleck. As a result, they observed no significant difference in the strength of tubes twisted one way and others twisted to the same stress in the opposite direction.

*2.2.2. $\sigma \rightarrow \gamma$ path*

Five tests were performed for this loading history in order to establish if this switch had any effect on the strength. The specimens were first compressed to a predetermined level ranging between approximately 60 and 118 ksi (414–807 MPa). This stress was then kept at a constant level while the specimen was sheared under displacement control. A typical set of results recorded in a test pre-compressed to 60.6 ksi (418 MPa) is shown in Fig. 5. Figure 5a shows the axial $\sigma - \delta/L$ response and Fig. 5b the $\tau - v^*/L$ response. The numbers in circles identify points on the responses with points on the loading history shown in the inset of Fig. 5a. The axial stress–strain response is nearly linear and relatively stiff. Its slope is smaller than $E_{11}$ because the displacement includes deformation of various parts of the testing set-up.

At ① the value of $\sigma$ is fixed and the specimen is sheared by prescribing $\dot{v}^*$. The shear response is seen to exhibit significant nonlinearity. Shearing tends to also shorten the specimen and $\delta$ is seen to grow between ① and ②. The tangent modulus gets progressively smaller and, eventually, a limit load is reached. Because of the relatively stiff nature of the test set-up, part of the descending response could be followed indicating that in this test failure was initially occurring in a controllable manner. The test was interrupted at ② by suddenly removing the shear load. Kinking initiated at the corner of the plate and progressed halfway across it at an inclination ($\beta$) of $11^\circ$ to the $x_2$-axis. As reported in Vogler and Kyriakides (1997), a kink band of this type has associated with it a lateral deflection $v$ (difference between position of material above and below the kink band) which, to a first order, can be approximated by

$$v = w \sin \phi \tag{2}$$

where $w$ is the width of the band and $\phi$ is the rotation of the fibers inside it. Since in this test $v^*$ is prescribed, the development of the kink band is inhibited to some degree resulting in the behavior observed.

The maximum shear recorded of 8.06 ksi (55.6 MPa) will be taken to be the critical shear stress at the

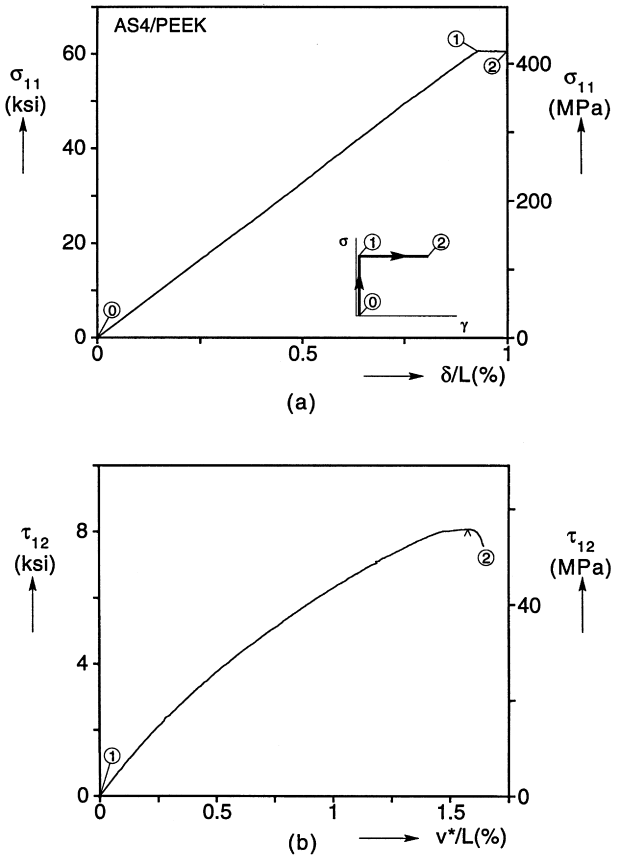


Fig. 5. Experimental results for a specimen tested under the $\sigma \rightarrow \gamma$ loading path. (a) Axial stress-end shortening response; (b) shear stress-horizontal displacement response.

axial stress of 60.6 ksi (418 MPa). The critical stresses from five tests performed under this loading history are plotted in the $\tau_\infty - \sigma_C$ plot in Fig. 4. Three of the points are somewhat lower than the corresponding points from the $\tau \rightarrow \varepsilon$ loading path while the other two almost coincide with their counterparts. In view of the scatter in the data, we conclude that the effect of loading path on the critical stresses is small if any.

The characteristics of the kink bands developed under biaxial loading were examined. The kink band inclinations varied from 10–15° which are somewhat lower than the values measured in similar plate tests under pure compression. However, no clear trend of the effect of $\tau$ on $\beta$ was found. The fiber rotation angles, $\phi$, inside the kink bands were generally smaller than the 30° values measured after the load was removed in kink bands formed under pure compression. Here, $\phi$ was on the order of 20°. Perhaps because of this smaller fiber rotation, the fibers bend and align themselves to the new orientation of $\phi$, in the main, without breaking. This is illustrated in the micrograph in Fig. 6 where the edge of such a kink band with straight fibers on one side and rotated fibers on the other can be seen.

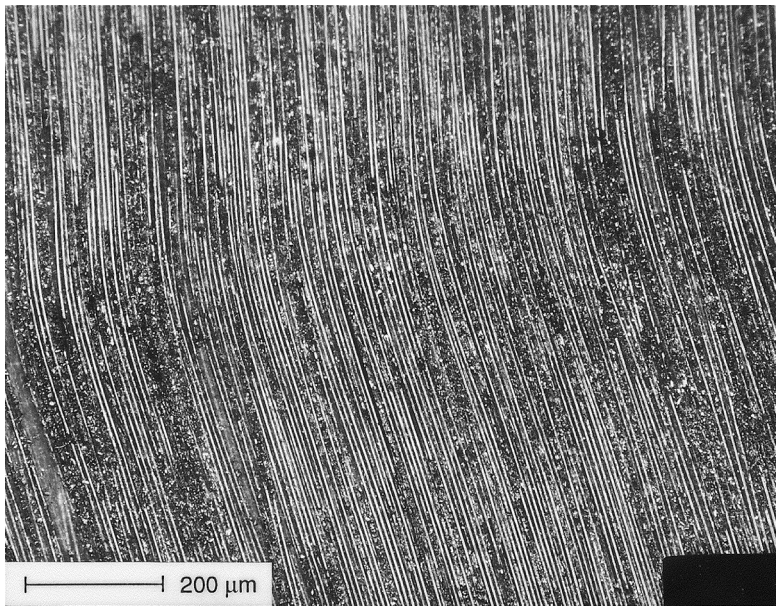


Fig. 6. Photomicrograph of a kink band formed in a specimen preloaded in compression to 60.5 ksi (417 MPa) and then sheared to failure.

## 3. Models

### 3.1. Large-scale micromechanical models

We now modify the two- and three-dimensional micromechanical models of fiber composites, used in the past to calculate the compressive response and strength, to handle the needs of the combined loading problem. In the two-dimensional model, the composite is idealized as an alternating array of fiber and matrix layers each of uniform thickness as shown in Fig. 7. The fiber thickness ($h$) is 7 $\mu$m. The thickness of the matrix is chosen to match the 0.60 fiber volume fraction of the material. The fibers have a sinusoidal imperfection along the $x_1$-direction with amplitude $a$ and wavelength $2\lambda$. For the purposes of the present study, the imperfection will be uniform across the width of the microsection and is expressed as

$$v_0 = a\cos\frac{\pi x_1}{\lambda}. \tag{3}$$

In the three-dimensional model the fibers are circular with diameter $h$ ($=7$ $\mu$m) and are distributed in a hexagonal arrangement in the matrix as shown in Fig. 8. The spacing of the fibers ($c$) is related to the fiber diameter and volume fraction ($v_f$) through

$$c = h\sqrt{\frac{\pi\sqrt{3}}{6v_f}}. \tag{4}$$

The fibers have the same sinusoidal imperfection in the $x_1 - x_2$ plane as the 2-D model. Because of the

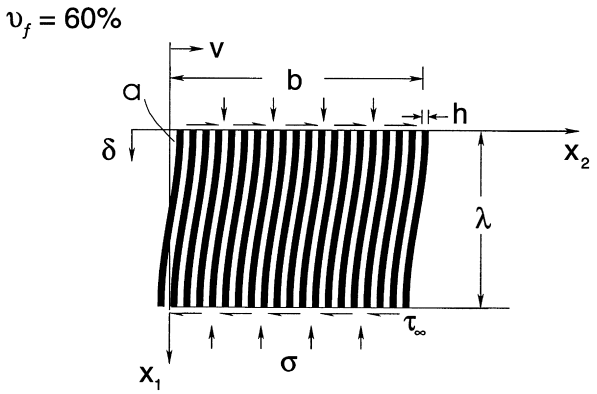


Fig. 7. Geometry of composite microsection idealized as a 2-D solid of alternating fibers and matrix with a sinusoidal imperfection. Microsection loaded in compression and shear.

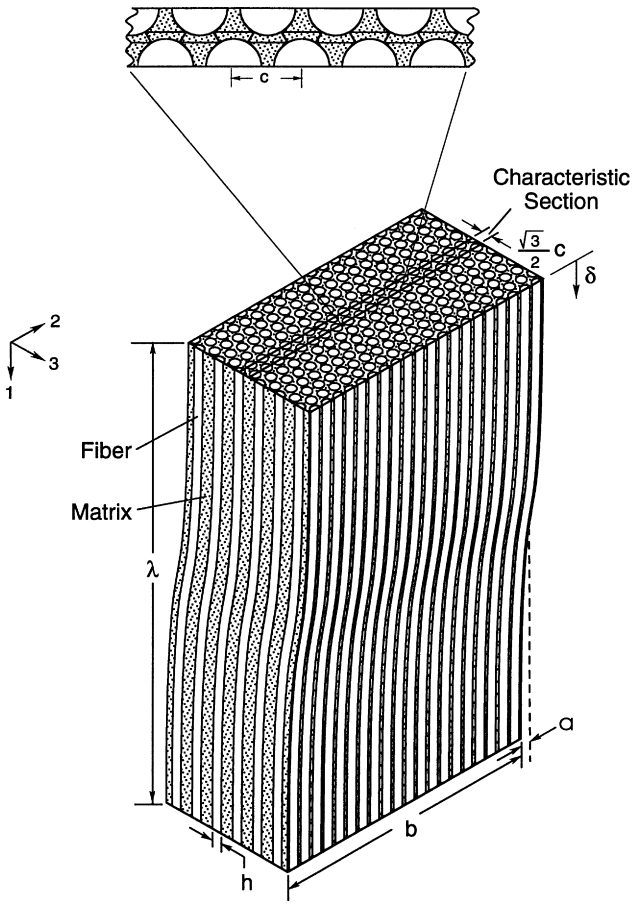


Fig. 8. Geometry of an idealized composite with a sinusoidal imperfection used in the 3-D FE model.

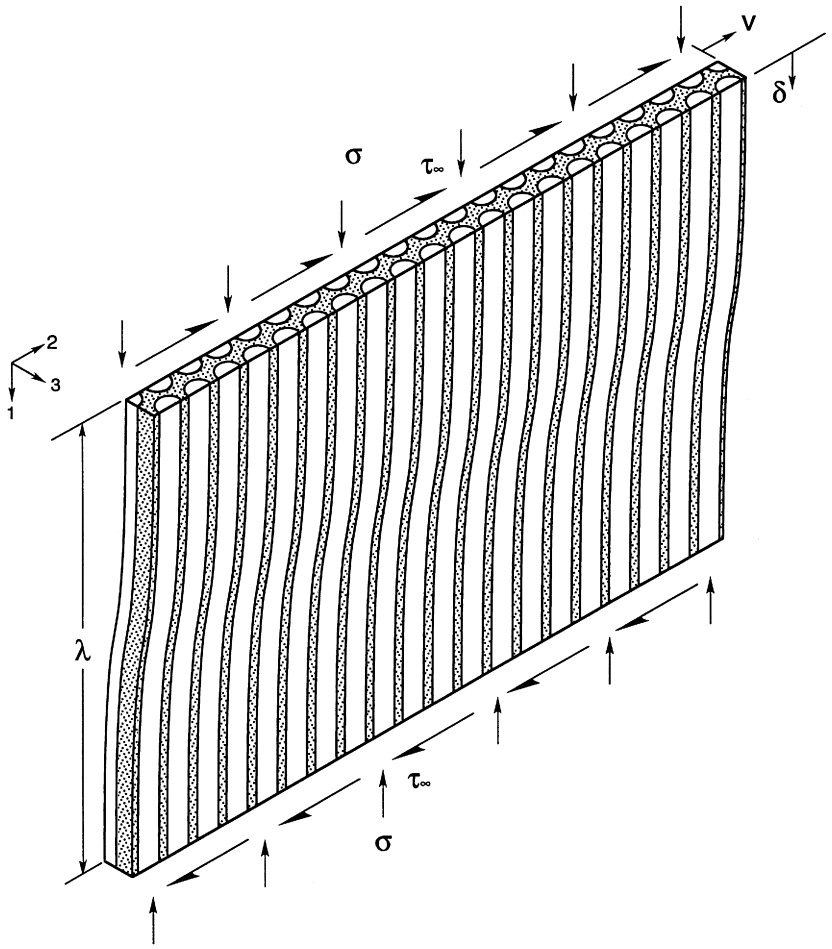


Fig. 9. Characteristic section of the idealized composite for the 3-D model loaded in compression and shear.

periodicity of the problem, it suffices to consider a representative slice of the material of width $\sqrt{3}c/2$ on whose lateral surfaces zero normal displacements are prescribed (see Fig. 9).

For pure axial loading the models were assumed to exhibit axial periodicity. With the addition of shear, periodicity is no longer invoked. Instead, we extract microsections one-half period long ($\lambda$) and with width $b$ defined by the number of fibers $n_f$ used. In both models the fibers and matrix are discretized with finite elements. Details about the discretizations were given in Kyriakides et al. (1995) and Hsu et al. (1998) and will not be repeated here. Axial loading is such that the top and bottom surfaces of the microsections in Figs. 7 and 9 remain plane. Shear is applied to the top of the model by prescribing the displacement $v(0,\bullet)$ of the center node (nodes for 3-D model). The displacement of other nodes on these surfaces are related to the prescribed displacement by

$$v(0,\bullet) = \frac{v_i + v_{-i}}{2} \tag{5}$$

Table 1
Material properties of the composite and its constituents
(a)

| APC-2/AS4 composite | | | | |
|---|---|---|---|---|
| $E_{11}$ msi (GPa) | $E_{22}$ msi (GPa) | $G_{12}$ msi (GPa) | $\nu_{12}$ | $\upsilon_f$ |
| 18.62 (128) | 1.533 (10.57) | 0.84 (5.79) | 0.3 | 60% |

(b)

| AS4 Fibers | |
|---|---|
| $E_f$ msi (GPa) | $\nu_f$ |
| 31.0 (214) | 0.263 |

(c)

| APC-2 (PEEK) Matrix | | | | | |
|---|---|---|---|---|---|
| 2-D Models | | | 3-D Model | | |
| $E_m$ ksi (GPa) | $\sigma_{om}$ ksi (MPa) | $\nu_m$ | $E_m$ ksi (GPa) | $\sigma_{om}$ ksi (MPa) | $\nu_m$ |
| 893 (6.14) | 11.9 (82.1) | 0.356 | 594 (4.10) | 9.5 (65.5) | 0.356 |

where $v_i$ is the displacement of a node $i$ to the right of the center, and $v_{-i}$ is its counterpart to the left of the center node. Because of the antisymmetry of the problem, it is possible to consider only half of the microsections shown in Figs. 7 and 9.

The sides of both models are free. As was the case in the experiments, this causes some nonuniformity in the axial stress as well as in the shear stress. This nonuniformity is reduced by making the aspect ratio of the microsection relatively large. Again, in order not to inhibit the development of localized bending along inclined bands, the aspect ratio could not be made too large. The microsections analyzed have a half wavelength of $\lambda = 75h$ and are 90 fibers wide. This yields an aspect ratio $(b/\lambda)$ of approximately 2 for the 2-D model and of approximately 1.48 for the 3-D model. The implications of these choices on the load nonuniformity will be examined in the results section.

Key components of these models are the constitutive properties adopted for the fibers and matrix. As in the past, we assume the fibers to be isotropic and linearly elastic with the properties given in Table 1. The matrix is modeled as a finitely deforming $J_2$-type elasto-plastic solid which hardens isotropically. The properties of the matrix in each model are extracted from a torsion test on a filament wound thin-walled tube of this material as follows. In each case a representative micromodel is loaded under pure shear (layered for 2-D, hexagonal fiber array in matrix for 3-D). The fibers are assigned the properties

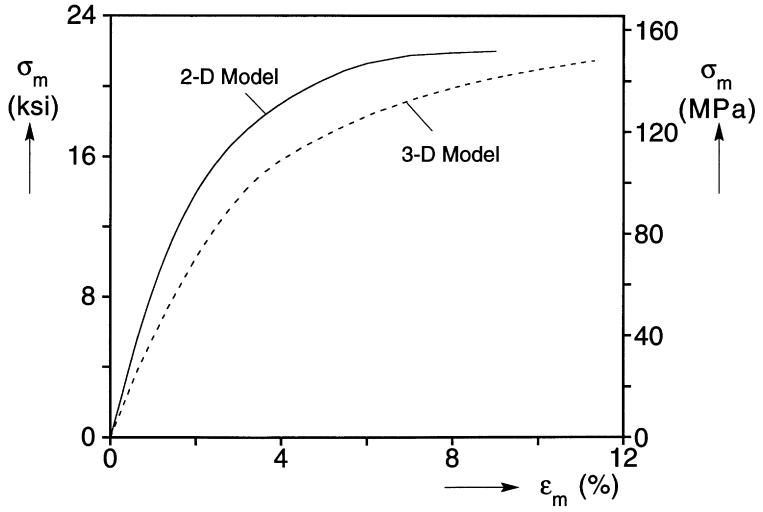


Fig. 10. PEEK stress–strain responses used in the 2-D and 3-D models.

in Table 1. The matrix properties are calculated iteratively such that each model composite matches the measured shear response (see Hsu et al., 1998). The two matrix stress–strain responses established in this manner are shown in Fig. 10. For strains higher than 9% in the 2-D case and 11% in the 3-D case, the stress–strain responses are assumed to be perfectly plastic. Fig. 11 shows a comparison of the measured shear response and those from the models using the extracted stress–strain responses. The one obtained from the 3-D model matches the stress–strain response measured in a uniaxial tension test on neat PEEK up to a strain of approximately 1.5% but is stiffer for higher strains. The inelastic behavior of this material is complex. For example, for neat material the stress–strain responses in shear, tension and compression are such that they can not be reproduced by $J_2$ isotropic hardening plasticity. In addition, it seems that the crystallinity of the material in the composite is different than in neat form due to the presence of the fibers. The calculation of strength under the present loading conditions is strongly dependent on the shear response of the composite. As a result, we consider the matrix stress–strain response extracted in the manner described above the most appropriate for the purposes of the calculations that follow. At the same time, due to the limitations of the plasticity model adopted, results far into the post-buckling regime will only be depended upon for qualitative behavior.

Under pure compression the critical load was shown to be very sensitive to imperfections. As we will see, this is also the case for compression in the presence of shear. One of the objectives of the present effort was to examine if this type of model can reproduce the strong interaction between compression and shear seen in the experiments. As mentioned above, the real composite has particular complex distributions of fiber imperfections which do not have a directional bias. In the models this will be represented by an 'equivalent' sinusoidal imperfection which has a direction bias. As a result, the shear must be applied in the direction that makes it 'cooperative' to the imperfection for it to cause a reduction in strength. The amplitude of the imperfection is chosen in a calibration calculation using the 2-D model so that the predicted strength corresponds to the average of the three compression strengths given above (178 ksi—1.228 GPa). The required amplitude was found to be $a = 0.87h$. The same value is used in the 3-D model.

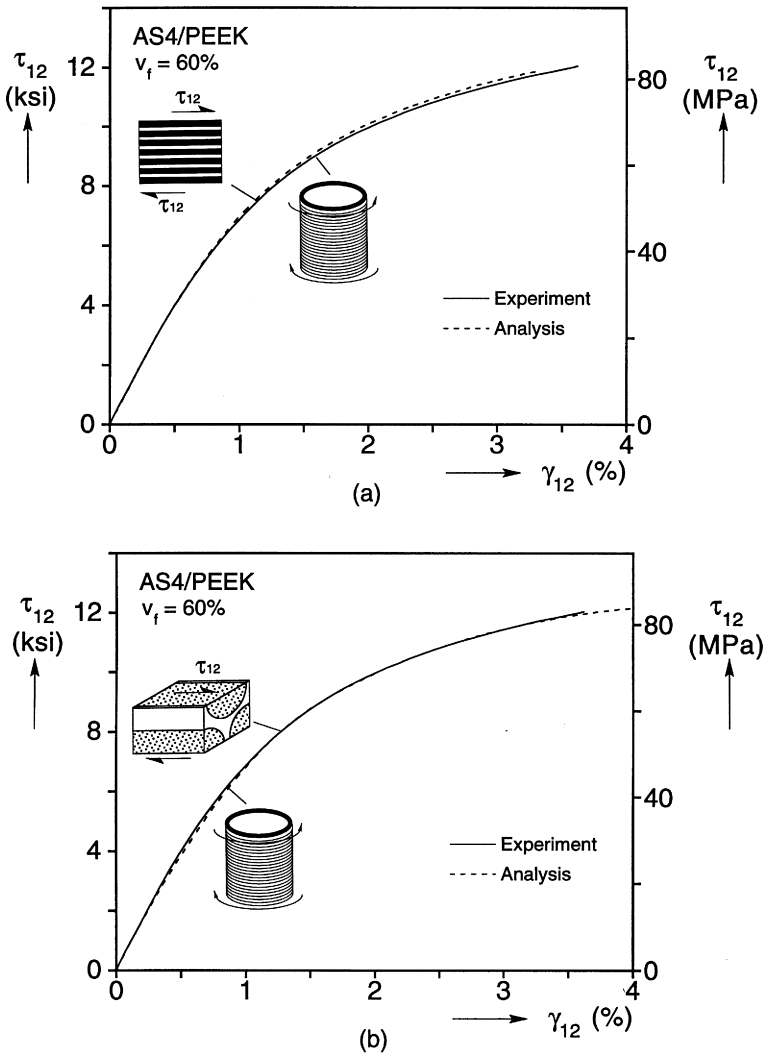


Fig. 11. Comparison of measured composite shear response to numerical simulations for (a) the 2-D model and (b) the 3-D model.

### 3.2. Straight inextensional fibers model

The numerical models described above include realistic representations of fiber extensionality, fiber bending and matrix nonlinearity. In the past, the models were also used to study the effect of realistic spatial distribution of fiber imperfections on strength. In addition to yielding dependable predictions of strength, they afford at least qualitative simulation of the localization process that leads to kink bands. However, if the objective is limited to predicting the compressive strength of composites with a uniform imperfection, the much simpler class of models of Budiansky (1983) and Budiansky and Fleck (1993) are a viable alternative (see also Schapery, 1995). In the simplest of these models the fibers are straight, inextensional and uniformly inclined to the direction of loading as shown in Fig. 1. (In all numerical

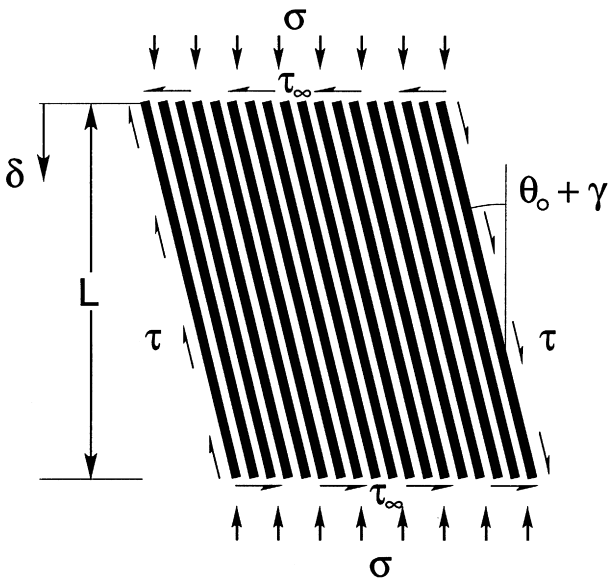


Fig. 12. Idealized composite used in the straight fibers model loaded in compression and shear.

simulations of kink band formation, the bands have been found to initially form in a direction normal to that of the applied stress. They become inclined at later stages of postfailure. It is for this reason that we opt to use the zero kink band inclination version of this model.) Hsu et al. (1998) showed that when $\tau(\gamma)$ is made to correspond to the measured shear response of the composite, the strengths predicted by eqn (1) for $\theta_o > 0.5^\circ$ are in very good agreement with those from our 2-D and 3-D numerical models.

Motivated by this, we examine the performance of the same model for compression in the presence of shear as shown in Fig. 12. Straight-forward transformation of stresses to an orthogonal frame along and normal to the fibers, together with the assumption that both $\theta_o$ and the induced shear strain ($\gamma$) are small, results in the following relationship

$$\sigma = \frac{\tau(\gamma) - \tau_\infty}{\theta_0 + \gamma}. \tag{6}$$

This corresponds to eqn (62) in Budiansky and Fleck (1993) derived for zero kink band inclination (the difference in the denominator is due to a rigid body rotation, $\gamma_\infty$, they applied to their model so that compression starts with the fibers aligned to the axial load). Once again $\tau(\gamma)$ is the shear response of the composite and $\gamma$ is the shear strain due to both applied stresses.

We 'calibrate' this model in the same way we calibrated the numerical models; that is, we choose an equivalent value of $\theta_0$ such that at zero shear stress the model yields the measured compressive strength of 178 ksi (1.228 GPa). For the composite shear response shown in Fig. 11, this required $\theta_0 = 0.0351$ (2.01°). Provided the sinusoidal imperfections used in the bending fibers models have long wavelengths and relatively small amplitudes, the uniform initial inclination of this model can be approximated by

$$\theta_0 \approx \frac{\pi a}{\lambda} \tag{7}$$

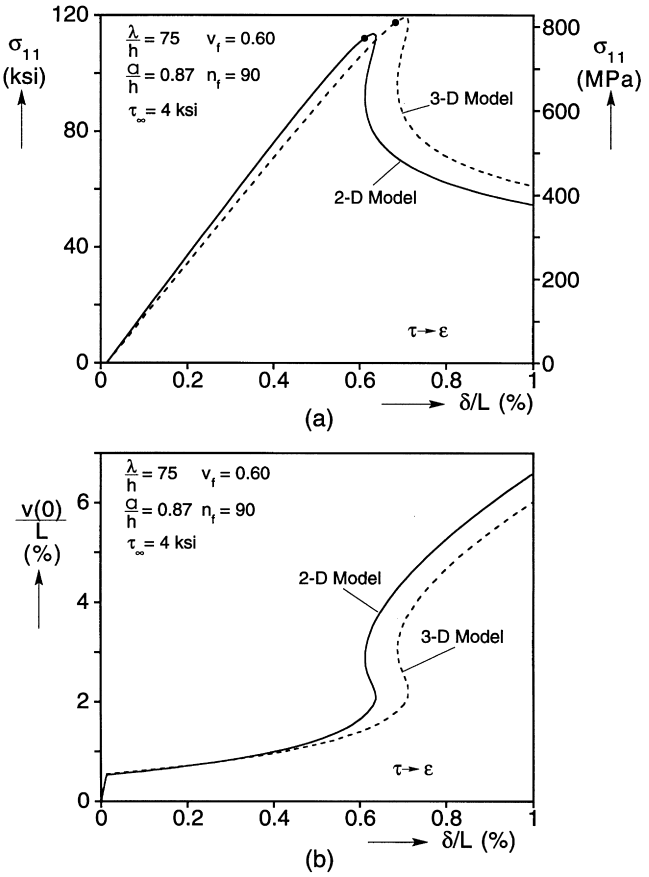


Fig. 13. Responses for the 2-D and 3-D models. (a) Axial stress-end shortening response; (b) horizontal displacement-end shortening response.

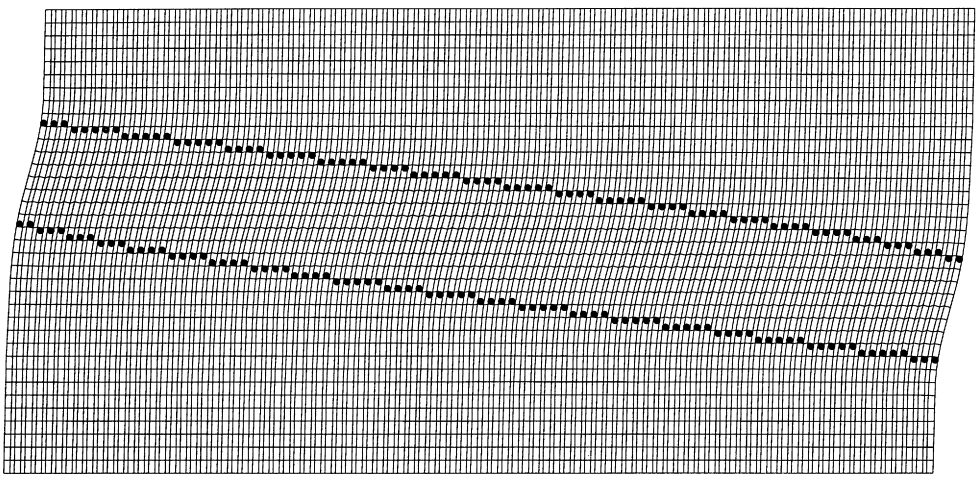

Fig. 14. Deformed configuration of the 2-D model corresponding to 1% end shortening for case shown in Fig. 13.

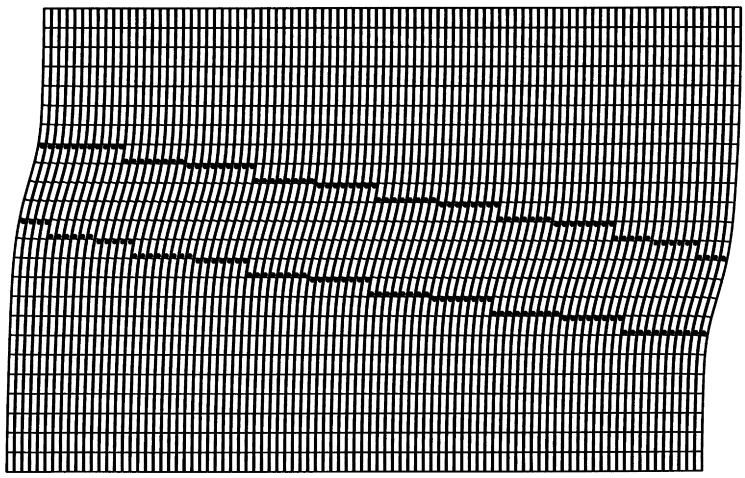

Fig. 15. Deformed configuration of the 3-D model corresponding to 1% end shortening for case shown in Fig. 13.

(Kyriakides et al., 1995). For $\lambda = 75h$ and $a = 0.87h$, eqn (6) yields $\theta_0 = 2.088^\circ$ which is in good agreement with the result from direct calculation.

## 4. Predictions

### 4.1. Large-scale micromechanical models

#### 4.1.1. A representative example

We first consider results obtained using the 2-D and 3-D micromechanical models. We will use results for the loading path $\tau \rightarrow \varepsilon$ with $\tau_\infty = 4$ ksi (27.6 MPa) as an illustrative example. The axial stress-displacement responses yielded by the two models are shown in Fig. 13a. The responses exhibit the same features as those from pure compression; they are initially stiff and almost linear with an elastic modulus close to that of the actual composite. As the axial stress increases, the matrix is plasticized and, as a result, the shear modulus is reduced. The biggest shear deformation and, correspondingly, the maximum reduction in shear modulus takes place in the middle of the microsections shown in Figs. 7 and 9 where the initial fiber rotations are most severe. For the load and imperfection orientations chosen, the far field shear and the shear induced by the axial stress have an additive effect. At some value of axial stress corresponding to the stress maximum of each response, the reduction in the shear modulus is high enough that the axial stress can no longer be supported and the microsections start to collapse. The critical stresses have values of 113.6 ksi (783.4 MPa) for the 2-D model and 119.2 ksi (822.1 MPa) for the 3-D model.

Subsequently, the responses exhibit the characteristic cusp-like behavior reported for pure compression in our previous works. Riks' path-following technique is used to trace this part of the response. The sequence of events that take place following the load maximum are similar to those reported for pure compression. With the net axial stress dropping, the deformation localizes into a narrow band in the center of each microsection. The band is initially horizontal but rotates and broadens at higher values of axial displacement. The behavior is qualitatively similar in the two models but the two responses deviate from each other as the details of the deformation are different in the two

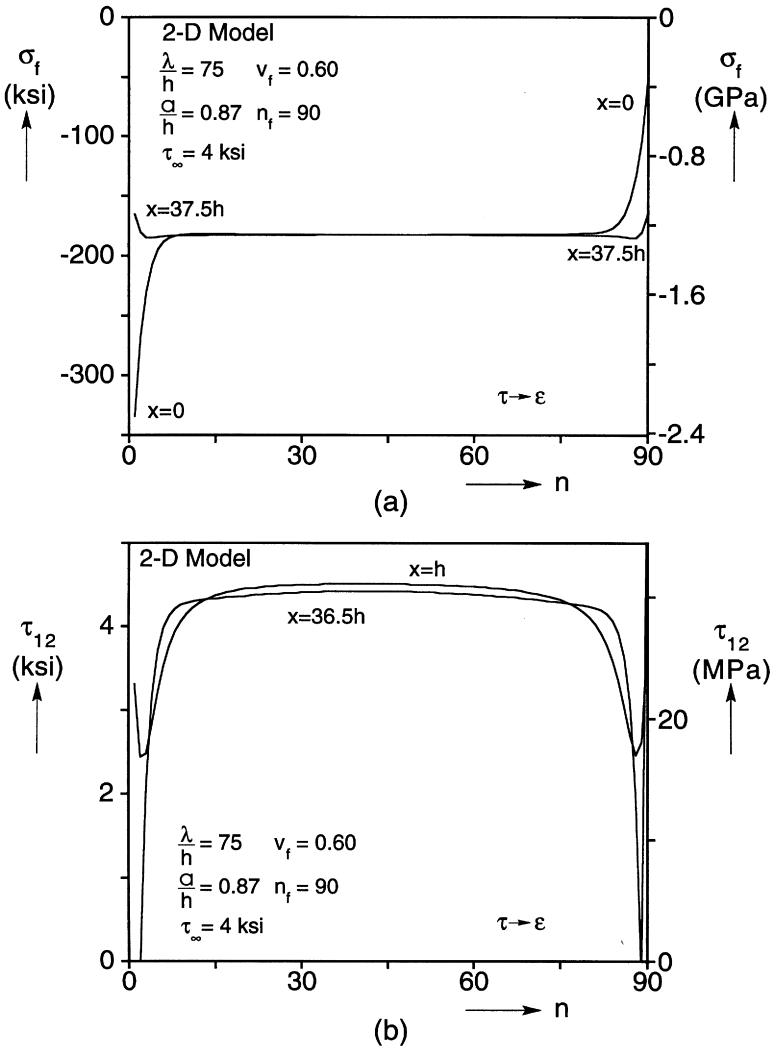


Fig. 16. Distribution of stress across the width of the 2-D model. (a) Axial stress in fibers; (b) shear stress in the composite.

microstructures. Figs. 14 and 15 show the bands in the 2-D and 3-D microsections at $\delta/L = 1\%$. Their inclinations to the $x_2$-axis are respectively 8° and 9°. Both are approximately 1° smaller than the corresponding inclinations for pure compression (see Fig. 7 in Hsu et al., 1998).

The net transverse displacements $v(0)$ of the microsections are plotted against the axial shortening in Fig. 13b. The variable $v(0)/L$ represents a gross measure of the shear deformation in the microsection although, as pointed out above, the shear strain at mid-height is larger than this value. The initial shear strain induced by $\tau_\infty$ is approximately 0.5%. As the axial stress increases the shear is seen to grow and, at the critical stress, reaches values of approximately 1.93 and 1.96% respectively for the 2-D and 3-D models. This is another illustration of the important role played by shear on failure. (Note that the shear at mid-height is approximately 1% higher than these values for both models.)

In the previous section it was mentioned that the finite width and free edges of the microsections are

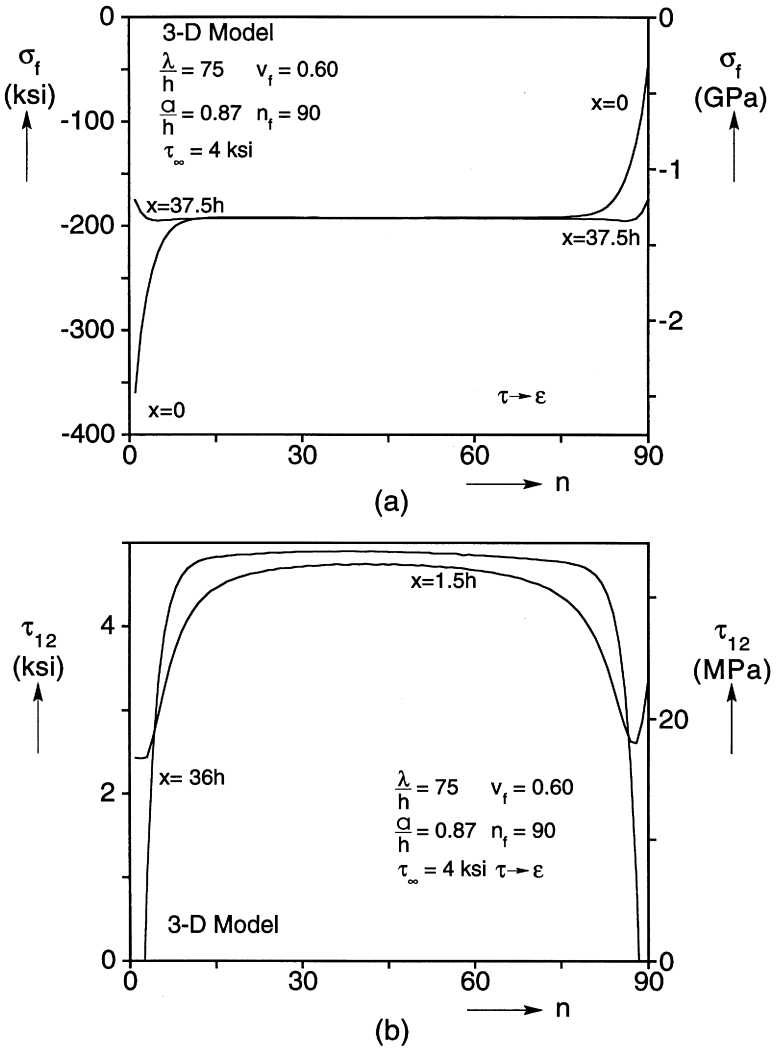


Fig. 17. Distribution of stress across the width of the 3-D model. (a) Axial stress in fibers; (b) shear stress in the composite.

expected to have some effect on the uniformity of the axial and shear stresses in the specimens. Fig. 16 shows plots of the average axial stresses in the individual fibers just before the limit load is achieved (marked with a • in Fig. 13a). The stresses shown correspond to the top surface of the microsection ($x = 0$) and to mid-height ($x = 37.5h$). The stresses are uniform in the interior but stress concentrations are seen to develop in boundary layers a few fibers wide on each free edge of the microsection. The stress concentration is much more pronounced at the top of the microsection whereas at mid-height it is much smaller. At $x = 0$ the boundary layers are approximately 5 fibers wide whereas at $x = 37.5h$ they are only 2 fibers wide.

The shear stress across the specimen at approximately the same axial locations is plotted in Fig. 16b ($\tau_{12}$ represents the shear stress suitably averaged over each fiber and its adjacent matrix elements). The shear at the top surface does not die to zero at the ends because this is where the shear load is applied

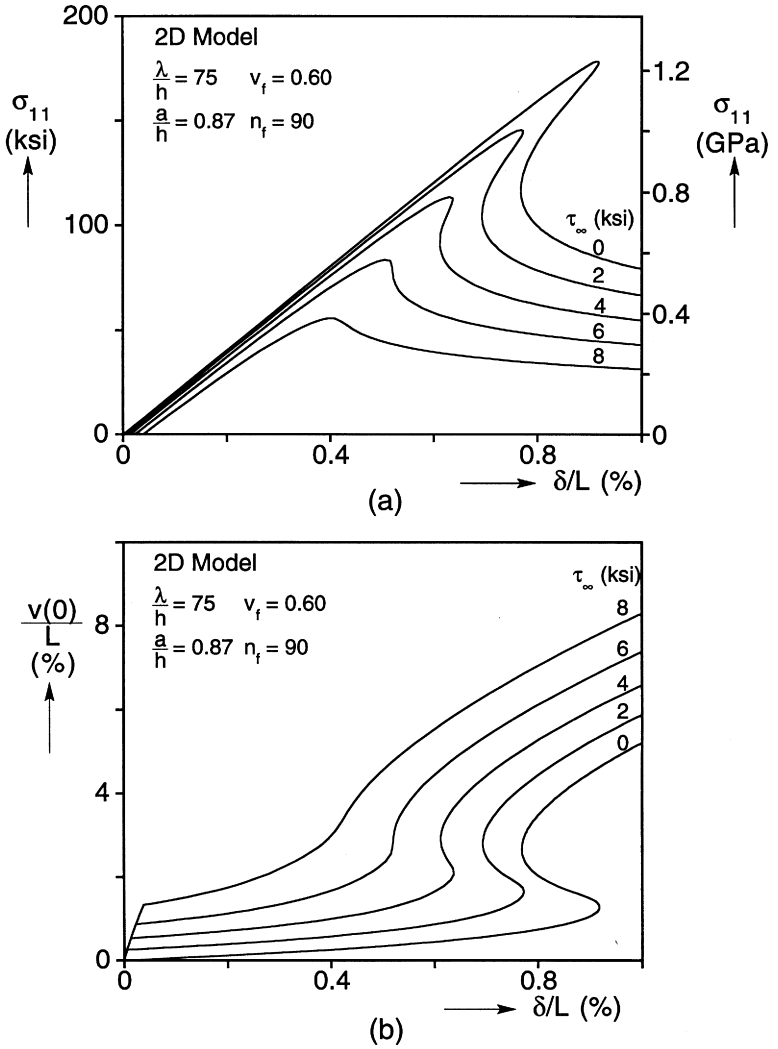


Fig. 18. Responses from the 2-D model for five values of applied shear. (a) Axial stress- end shortening response; (b) horizontal displacement-end shortening response.

and because of the way the stress is averaged. At the microsection mid-height the shear distribution is more uniform in the interior and dies to zero in boundary layers approximately 5 fibers wide.

Similar stress distributions extracted from the 3-D model are shown in Fig. 17. The more complex microstructure of this model and its smaller width result in somewhat more extended boundary layers, but otherwise the results are very similar to those in Fig. 16. The axial and shear stress distributions are again markedly more uniform at the microsection mid-height.

As mentioned earlier, the choice of the width of the microsections in the present calculations was driven by postfailure considerations. In the later stages of the failure process, the band of highly bent fibers becomes inclined. In order not to interfere with this process the band should not run into the top or bottom edges of the microsection. This imposes limitations on the microsection width. However, if

Table 2
Calculated critical stresses, axial strains and shear strains at various values of shear stress[a]

| $\tau_\infty$ ksi (MPa) | $\sigma_C$ ksi (MPa) | | $\varepsilon_c$% | | $\frac{v_c(0)}{L}$% | |
|---|---|---|---|---|---|---|
| | 2-D | 3-D | 2-D | 3-D | 2-D | 3-D |
| 0 | 178.4 (1230) | 183.1 (1263) | 0.91 | 1.01 | 1.17 | 1.27 |
| 2 (13.8) | 145.5 (1003) | 150.2 (1036) | 0.77 | 0.85 | 1.54 | 1.58 |
| 4 (27.6) | 113.6 (783) | 119.2 (822) | 0.63 | 0.70 | 1.93 | 1.96 |
| 6 (41.4) | 83.7 (577) | 90.5 (624) | 0.51 | 0.58 | 2.37 | 2.5 |
| 8 (55.2) | 55.7 (384) | 63.9 (441) | 0.40 | 0.49 | 2.92 | 3.33 |
| −4 (−27.6) | 254.3 (1754) | — | 1.265 | — | 0.635 | — |

[a] $\frac{\lambda}{h} = 75$, $\frac{a}{h} = 0.87$.

we limit the objectives of the analysis to just finding the critical stress, then no limitations on the microsections width need be imposed. In view of this, we performed convergence studies on the effect of $n_f$ on the calculated critical stress for $\tau_\infty = 4$ ksi (27.6 MPa). We found that doubling the width increased the critical stress by approximately 1.5%. Clearly, the critical stress is associated with the collapse of the whole specimen and, as a result, the edge effects do not play as big a role on its value.

*4.1.2. Summary of numerical results*

Calculations of this type were performed at 2 ksi (13.8 MPa) increments of $\tau_\infty$ in the range of 0 to 8 ksi (0–55.2 MPa) using both models. The axial stress-displacement responses from the 2-D calculations are shown in Fig. 18a. The corresponding transverse displacement-axial displacement responses are shown in Fig. 18b. The critical stresses and strains are listed in Table 2. The results clearly show that the application of a far field shear stress reduces drastically the critical axial stress. Indeed, the set of axial responses shown in Fig. 18 are reminiscent of similar results for $\tau_\infty = 0$ but with the amplitude of the initial imperfection as the parameter varied (e.g., see Fig. 23b in Kyriakides et al., 1995; Fig. 17 in Kyriakides and Ruff, 1997; Fig. 11 in Hsu et al., 1998). Because the composite shear response is nonlinear, the application of a constant shear stress is not quantitatively equivalent to a proportional increase in the imperfection. However, a qualitative equivalence between the two variables can still be claimed.

The same calculations were also performed with the 3-D model. The responses are similar to those in Fig. 18 and will not be shown here. The critical stresses and strains obtained are listed in Table 4. The small difference between critical stresses from the 2-D and 3-D models which was present for $\tau_\infty = 0$ is maintained at all values of shear stress. However, the trend in the two sets of results is very similar indeed. In the post-failure regime the bands of localized fiber bending were similar to those seen in pure compression with the general trend being that at a given value of $\delta/L$ the inclinations of the bands in the presence of far field shear are somewhat smaller.

The calculated critical stresses are plotted against $\tau_\infty$ in Fig. 4 together with the experimental results. The predicted failure envelopes are almost linear and nearly parallel with the 2-D results being somewhat lower. Overall, the predictions follow the trend of the experimental points, most of which lie above the calculated envelopes. This agreement indicates that the models developed and the method used to calibrate them are reliable tools for establishing such interaction failure envelopes.

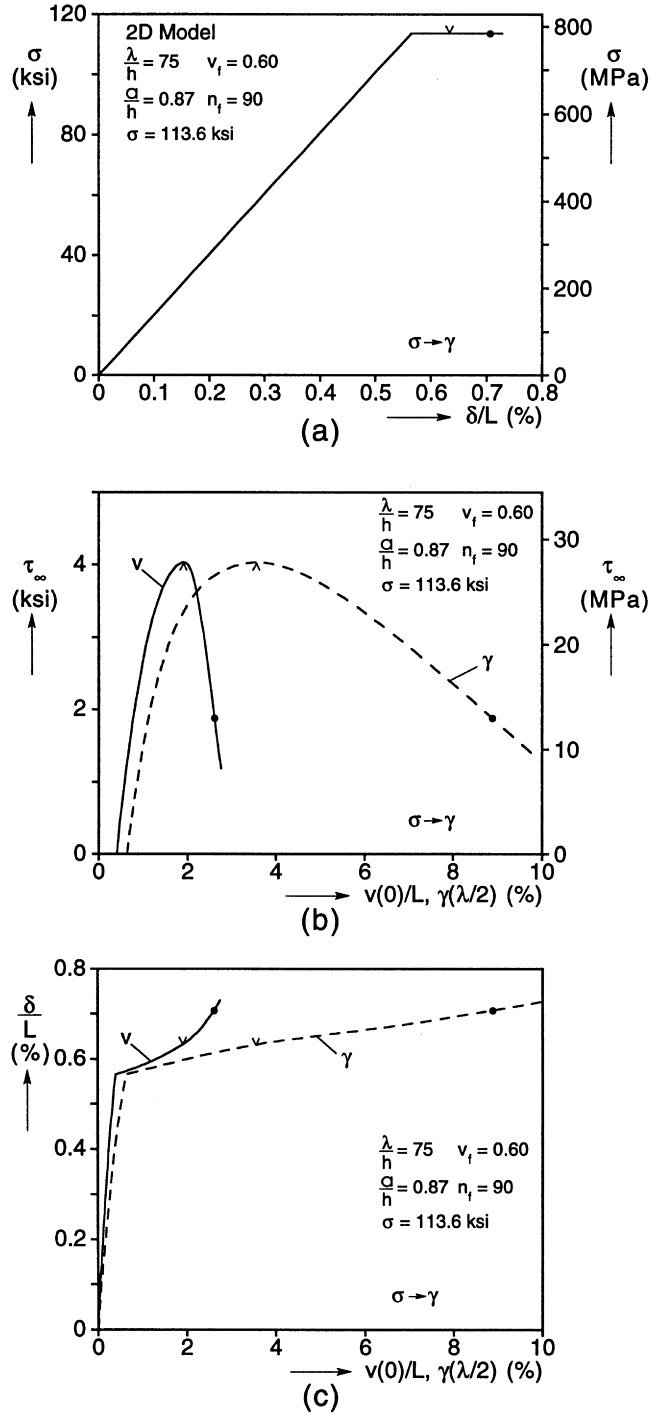


Fig. 19. Response for 2-D model for the $\sigma \rightarrow \gamma$ loading path. (a) Axial stress-end shortening response; (b) $\tau_\infty - v(0)/L$ and $\tau_\infty - \gamma(\lambda/2)$ responses; (c) end shortening vs $v(0)/L$ and $\gamma(\lambda/2)$.

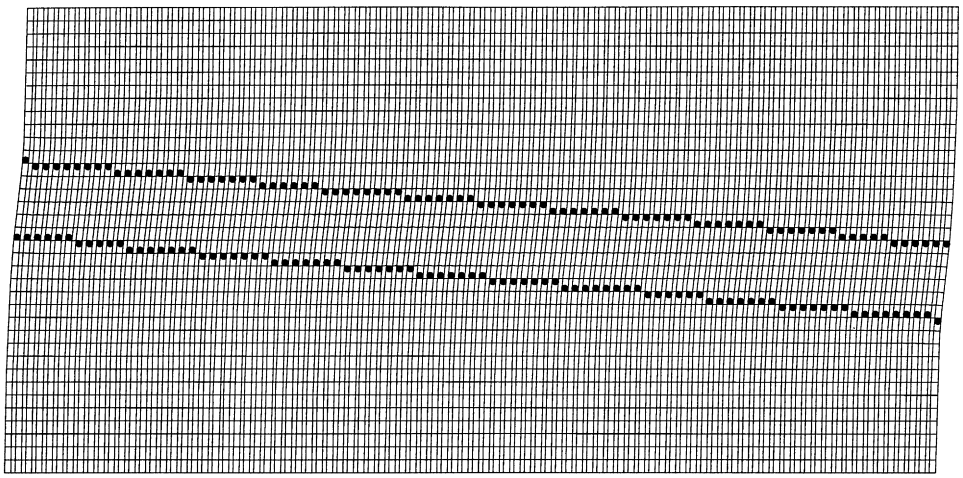

Fig. 20. Deformed configuration of the 2-D model corresponding to points identified by • in the responses in Fig. 19.

*4.1.3. Other loading paths*

Several calculations were also performed for the $\sigma \rightarrow \gamma$ loading path. A representative set of results from the 2-D model is shown in Fig. 19. The axial stress is first increased to the level of 113.6 ksi (783 MPa) which corresponds to the critical stress calculated for the $\tau \rightarrow \varepsilon$ path for $\tau_\infty = 4$ ksi (27.6 MPa, Table 4). The axial response (Fig. 19a) is essentially linear although the microsection shortens and shears as shown in Fig. 19c. The stress is fixed at this value and the specimen is then sheared by incrementally applying a horizontal displacement to the top surface ($v(0)$) as described in §3*a*. The shear stress that develops is plotted against the applied displacement in Fig. 19b. Plots of $\tau_\infty$ and $\delta/L$ vs the shear strain at $x = \lambda/2$ are also included in Fig. 19b and c ($\gamma(\lambda/2)$ is the average shear strain over a suitable domain in the center of the microsection). The shear stress is seen to rise nonlinearly to a maximum value of 4.03 ksi (27.8 MPa) and then drop. As expected, the shear strain at $x = \lambda/2$ is significantly higher than $v(0)/L$ which is more representative of the average shear strain in the microsection. The maximum shear achieved will be taken to be the critical failure stress. Thus, we see that the switch in the order the two loads are applied has a very small effect on the critical combination of $\tau_\infty$ and $\sigma$. This insensitivity to the loading path was also found to hold for other combinations of the two stresses in the range of interest. For imperfections of smaller amplitude, the sensitivity to loading path was found to increase somewhat but it remained too small to be of practical importance.

Following the shear stress maximum, deformation localizes into a distinct narrow band around the mid-height of the microsection. As a result of this localization, the growth of shear strain inside the band accelerates (see plots of $\gamma(\lambda/2)$ in Fig. 19b and c). As before, the band starts horizontal but broadens and rotates at higher values of $v(0)$. Fig. 20 shows the deformed microsection corresponding to the points marked with a solid bullet on the three responses in Fig. 19. At this stage of the loading history the band is $11.6h$ wide and has an inclination of 5°. The main difference in events versus those of the $\tau \rightarrow \varepsilon$ loading path is that here the applied displacement remains monotonically increasing; in other words, the postfailure is more controllable. This characteristic enabled us to follow the loading history beyond the shear stress maximum in some of the experiments. In the calculations the response can be followed down to a zero shear stress. The experiments were usually interrupted before this occurred in order to limit the extent of deformation in the kink bands that developed.

In summary, the interaction of the two stresses in the $\sigma \rightarrow \gamma$ loading path is as follows. The initial

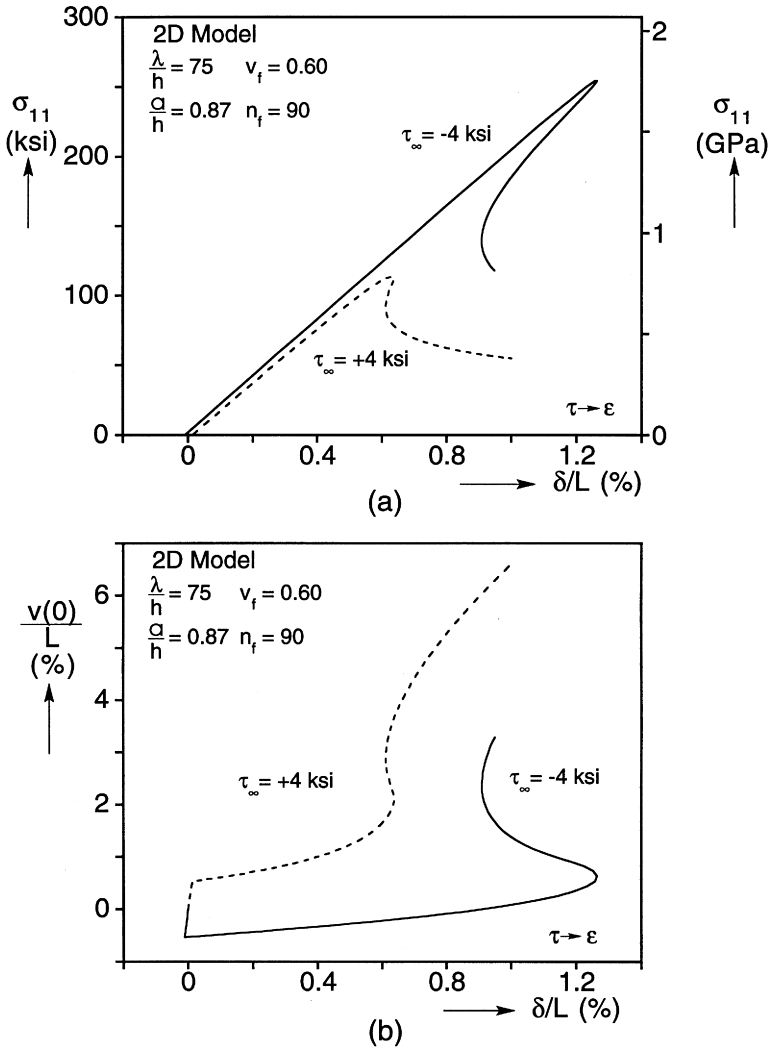


Fig. 21. Response of the 2-D model with positive and negative shear applied. (a) Axial stress-end shortening responses; (b) horizontal displacement-end shortening responses.

axial stress causes an increase in the shear deformation in the area of the microsection with the highest fiber misalignment. The axial stress is not sufficient to reduce the local shear modulus down to the level that results in failure. The application of far field shear continues the plastification of the material and the degradation in the local shear modulus. Eventually, at $\tau_\infty = 4.03$ ksi (27.8 MPa), the shear modulus degrades enough that shear deformation no longer requires increase in shear stress and the microsection starts to collapse. Unlike the alternate loading path, here, it can only collapse at the rate $v(0)$ is increased.

*4.1.4. Effect of imperfection bias*

In all the calculations reported thus far the microsections were sheared in a sense that was 'cooperative' to the geometric imperfection of the fibers ($\tau_\infty > 0$). In order to illustrate further the way

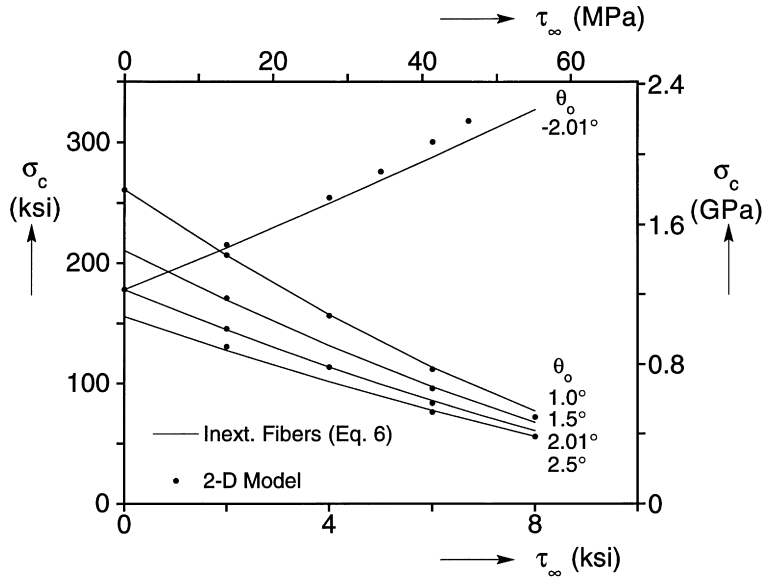


Fig. 22. Compressive strength under shear loading for four values of initial imperfection.

the fiber imperfections and far field shear interact, we conducted several calculations in which the microsections were sheared in a sense that is 'uncooperative' to the imperfection ($\tau_\infty < 0$). Results for $\tau_\infty = \pm 4$ ksi ($\pm$ 27.6 MPa) and for the same fiber imperfection are compared in Fig. 21. Reversing the direction of the shear stress increases the critical axial stress to 254.3 ksi (1.754 GPa) a level which is nearly 2.4 times the critical stress for $\tau_\infty = +4$ ksi and even 43% higher than the critical stress under pure compression. This trend indicates that in practical applications in which the direction of shearing is fixed, a purposely designed small uniform misalignment of the composite in the opposite sense to the shear can have significant strengthening effect. Or, equivalently, if the composite is misaligned in a uniform manner, the application of a shear pre-load can increase the axial strength.

### 4.2. Straight inextensional fibers model

The simple model of Budiansky and Fleck (1993) in the form of eqn (6) is now used to generate the $\sigma_C - \tau_\infty$ failure envelope corresponding to the experiments and predictions in Fig. 4. The measured shear response of the composite (Fig. 11) is used directly in $\tau(\gamma)$ in the numerator of the equation. The composite is assumed to have a uniform equivalent inclination corresponding to the 'calibration' value of 2.01° (§3b). The failure envelope generated is shown in Fig. 4 (for values of $\tau_\infty > 6$ ksi the more accurate version of this equation in which angles are not assumed to be small was adopted). The failure envelope is almost coincident with the corresponding results generated by the 2-D FE model. This demonstrates once more the soundness of the reasoning behind this model.

Eqn (6) and the 2-D FE model are now used to generate $\sigma_C - \tau_\infty$ failure envelopes for misalignment angles ($\theta_0$) of 1°, 1.5° and 2.5°. The results are shown in Fig. 22. The first observation is that the numerical results are almost coincident with the predictions. This was the case for pure compression also provided the imperfection was larger than 1° (Hsu et al., 1998). The second observation is that the failure envelope steepens as $\theta_0$ decreases indicating a more severe sensitivity to far field shear.

Finally, the model was used to analyze the strengthening effect that results from having $\tau_\infty$ act opposite to the imperfection. This is achieved by making $\theta_0$ negative in eqn (6). Results for $\theta_0 = -2.01$ are included in Fig. 22. Equation (6) predicts that the strengthening effect seen for the case of $\tau_\infty = -4$ ksi in Fig. 21 carries to all values of shear. In this case, results from the 2-D FE model deviate somewhat from those of equation (6) for $\tau_\infty > 5$ ksi.

## 5. Conclusions

The effect of far field shear on the compressive strength of aligned fiber composites has been studied through a combination of experiments and analysis. Thin plates of an AS4/PEEK composite with aspect ratio of approximately 1.7 were tested to failure in a custom axial compression-shear testing facility. Experiments were conducted under two loading paths, $\sigma \rightarrow \gamma$ and $\tau \rightarrow \varepsilon$. Shear interacts strongly with compression producing a failure envelope which follows approximately a diagonal line joining the strengths on the two axes of the failure envelope (pure compression and pure shear). No significant difference between the failure stresses from the two loading paths was observed. For the $\tau \rightarrow \varepsilon$ loading path the specimens failed catastrophically leaving behind one or two inclined kink bands in the plane of the plate. For the $\sigma \rightarrow \gamma$ loading path failure initiated at a limit load in the shear stress. Because of the displacement controlled manner in which the shear was applied in this loading path, events beyond the shear maximum could be followed. Failure was again in the form of one inclined kink band. In both sets of tests the inclinations of the kink bands ranged between 10–15°. In the presence of far field shear the fibers inside the kink bands mainly bent and rotated without breaking. By contrast, under pure compression most fibers broke at the edges of kink bands.

The 2-D and 3-D FE models we used in the past to simulate failure under pure compression were extended to handle combined loading. The inelastic properties of the matrix were again selected such that both models match the shear response of the actual composite. In both models the fibers were assumed to have a sinusoidal imperfection which is uniformly distributed across the microsections analyzed. The amplitude of the imperfection was selected so that the models yield a critical stress for pure compression which matches the mean of the measured values. The two models were found to capture the interaction of the two stresses very well. The failure envelopes produced by both models approximately bound the experimental results from below. As in the experiments, no significant effect of the loading path on the critical stresses was observed. The models were used to explore and understand the postfailure events and the development of zones of localized fiber bending.

The simplest straight fibers model of Budiansky and Fleck (1993), calibrated in the same manner as the numerical models, was used to predict the critical strength of our composite as a function of the far field shear stress. The interaction failure envelope produced is in very good agreement with the corresponding numerical predictions.

The calculations showed that for a unidirectional composite loaded in shear and compression, a small uniform rotation in the opposite sense to the induced shear strain can have a significant strengthening effect. Equivalently, if a composite is uniformly misaligned to the direction of applied compression, the application of a shear pre-load in a sense that reduces the misalignment angle can have a similar strengthening effect.

## Acknowledgements

The financial support of the Office of Naval Research under contract N00014-91-J-4091 is

acknowledged with thanks. The work of TJV was also supported by the Fannie and John Hertz Foundation and the W.M. Keck Foundation.

## References

Argon, A.S., 1972. Fracture of composites. In: Herman, H. (Ed.), Treatise on Material Science and Technology, vol. 1. Academic Press, New York, pp. 79–114.

Budiansky, B., 1983. Micromechanics. Computers and Structures 16, 3–12.

Budiansky, B., Fleck, N.A., 1993. Compressive failure of fiber composites. J. Mechanics and Physics of Solids 41, 183–211.

Chatterjee, S.N., McLaughlin, P.V., 1979. Inelastic shear instability in composite materials under compression. Proc. 3rd ASCE Eng. Mech. Div. Specialty Confer. 17–19 September, University of Texas at Austin, 649–653.

Hsu, S.-Y., Vogler, T.J., Kyriakides, S., 1998. Compressive strength predictions for fiber composites. ASME J. of Applied Mechanics 65 (1), 7–16.

Jelf, P.M., Fleck, N.A., 1994. The failure of composite tubes due to combined compression and torsion. Journal of Materials Science 29, 3080–3084.

Kyriakides, S., Arseculeratne, R., Perry, E.J., Liechti, K.M., 1995. On the compressive failure of fiber reinforced composites. Int'l J. Solids and Structures 32 (6/7), 689–738.

Kyriakides, S., Ruff, A.E., 1997. Aspects of failure and postfailure of fiber composites in compression. J. Composite Materials 30 (20), 2000–2037.

Schapery, R.A., 1992. Analysis of local buckling in viscoelastic composites. In: Reddy, J.N., Reifsnider, K.L. (Eds.), Local Mechanics Concepts for Composite Material Systems, Proc. IUTAM Symposium, Blacksburg, VA, October 1991. Springer-Verlag, New York, pp. 229–250.

Schapery, R.A., 1995. Prediction of compressive strength and kink bands in composites using a work potential. Int'l J. Solids and Structures 32 (6/7), 739–765.

Slaughter, W.S., Fleck, N.A., Budiansky, B., 1993. Compressive failure of fiber composites: the roles of multiaxial loading and creep. ASME J. Eng. Materials and Techn. 115, 308–313.

Vogler, T.J., Kyriakides, S., 1997. Initiation and axial propagation of kink bands in fiber composites. Acta Materialia 45 (6), 2443–2454.

Vogler, T.J., Kyriakides, S., 1998. On the effect of loading rate on the compressive strength of an AS4/PEEK composite. ASME J. of Applied Mechanics 65 (4), 1056–1058.